A Mapping-Based Design for Nonsubsampled Hourglass Filter Banks in Arbitrary Dimensions

Yue M. Lu, *Member, IEEE*, and Minh N. Do, *Senior Member, IEEE*

***Abstract*—Multidimensional hourglass filter banks decompose the frequency spectrum of input signals into hourglass-shaped directional subbands, each aligned with one of the frequency axes. The directionality of the spectral partitioning makes these filter banks useful in separating the directional information in multidimensional signals. Despite the existence of various design techniques proposed for the 2-D case, to our best knowledge, the design of hourglass filter banks in 3-D and higher dimensions with finite impulse response (FIR) filters and perfect reconstruction has not been previously reported. In this paper, we propose a novel mapping-based design for the hourglass filter banks in arbitrary dimensions, featuring perfect reconstruction, FIR filters, efficient implementation using lifting/ladder structures, and a near-tight frame construction. The effectiveness of the proposed mapping-based design depends on the study of a set of conditions on the frequency supports of the mapping kernels. These conditions ensure that we can still get good frequency responses when the component filters used are nonideal. Among all feasible choices, we then propose an optimal specification for the mapping kernels, which leads to the simplest passband shapes and involves the fewest number of frequency variables. Finally, we illustrate the proposed techniques by a design example in 3-D, and an application in video denoising.**

***Index Terms*—Directional decomposition, directional filter banks, filter design, hourglass filter banks, multidimensional transforms.**

I. Introduction

TWO-DIMENSIONAL (2-D) filter banks with hourglass-shaped passband supports have been extensively studied in the past [1]–[6]. As shown in Fig. 1(a), these filter banks decompose the 2-D frequency spectrum into two hourglass-shaped subbands, whose dominant directions are aligned with the two frequency axes. The directionality of the passband supports makes the hourglass filter banks, also commonly known as the fan filter banks, useful in analyzing the directional information in 2-D signals. Furthermore, these filter banks serve as important building blocks of the widely used 2-D directional filter banks [7]–[9], which achieve higher angular resolution through a tree-structured concatenation of the hourglass filter banks together with resampling operations.

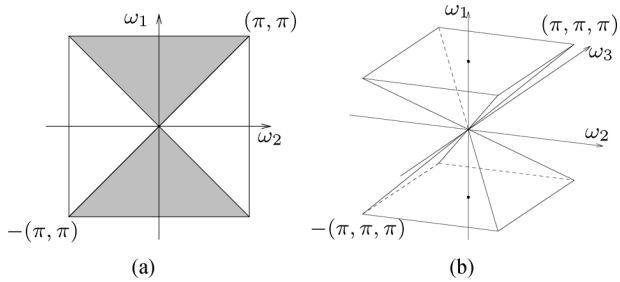

Fig. 1. (a) The frequency partitioning of 2-D hourglass (a.k.a. fan) filter banks. (b) The frequency support of one of the 3-D hourglass filters. The passbands of the other two hourglass filters are just rotated versions of this one.

In this paper, we study the hourglass filter banks in higher dimensions. In 3-D, for example, the proposed filter banks divide the spectrum into three directional subbands, whose 3-D hourglass-shaped passband supports [shown in Fig. 1(b)] are natural extensions of their 2-D counterparts [Fig. 1(a)]. In the general d-D ($d \geq 2$) case, the proposed hourglass filter banks decompose signals into d directional subbands, whose passband supports will be made precise in Section II.

Due to the shape of their frequency partitioning, the proposed hourglass filter banks can effectively decompose multidimensional signals into directional subbands aligned with different frequency axes. As shown in Fig. 2, the analysis/synthesis filter bank structure allows different directional subbands to be processed (e.g., enhanced or suppressed) independently, and then recombined together at the reconstruction stage. Furthermore, if the hourglass filter banks satisfy perfect reconstruction, then there is no signal distortion in the absence of subband processing.

There is one more motivation for the study of multidimensional hourglass filter banks. Analogous to the 2-D case, the hourglass filter banks in 3-D and higher dimensions are found to be important ingredients in the recently proposed multidimensional directional filter banks (NDFB) [10], which decompose signals into "thinner" directional subbands by using the hourglass filter banks followed by an iterative tree-structured filter bank. The resulting subband filters of NDFB are supported on rectangular-based pyramid-shaped regions, which radiate out from the origin at 3×2^l ($l \geq 0$) different orientations and tile the entire frequency space. Previous studies [11]–[13] have shown that multidimensional filters with similar type of directional passbands can be useful in a wide range of applications, including video processing, and seismic imaging.

Manuscript received December 20, 2006; revised July 12, 2007. This work was supported by the US National Science Foundation under Grant CCR-0237633 (CAREER). The associate editor coordinating the review of this manuscript and approving it for publication was Dr. Thierry Blu.

Y. M. Lu was with the Department of Electrical and Computer Engineering and the Coordinated Science Laboratory, University of Illinois at Urbana-Champaign, Urbana IL 61801 USA. He is now with the Audio-Visual Communications Laboratory, Swiss Federal Institute of Technology Lausanne (EPFL), Lausanne, Switzerland. (e-mail: yue.lu@epfl.ch).

M. N. Do is with the Department of Electrical and Computer Engineering, the Coordinated Science Laboratory, and the Beckman Institute, University of Illinois at Urbana-Champaign, Urbana, IL 61801 USA (e-mail: minhdo@uiuc.edu).

Color versions of one or more of the figures in this paper are available online at http://ieeexplore.ieee.org.

Digital Object Identifier 10.1109/TSP.2007.909340

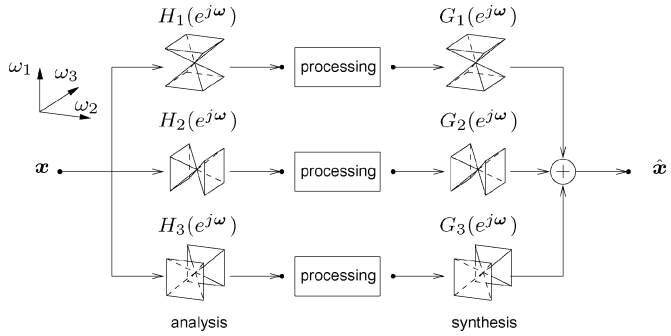

Fig. 2. The nonsubsampled hourglass filter bank in 3-D. The ideal frequency-domain supports of the component filters are hourglass-shaped regions, with their corresponding dominant directions aligned with the ω_1, ω_2, and ω_3 axes, respectively. Note that there is no sampling operation in the filter bank.

Fig. 2 shows the block diagram of the proposed hourglass filter banks in 3-D. We can observe that, unlike traditional critically sampled filter banks, the hourglass filter banks discussed in this paper are nonsubsampled, i.e., without downsampling or upsampling operations. This difference in filter bank structure is in part due to the following fact [14], [15]: it is impossible to implement the multidimensional hourglass-shaped frequency partitioning with a *critically sampled* filter bank, except for the 2-D case. Another important reason for us to consider this redundant construction is that the lack of sampling operations in the hourglass filter banks appears to be crucial in simplifying the design of subsequent iterative filter banks needed in the multidimensional directional filter banks. We refer to [10] for details.

Various design techniques have been proposed in the literature for the hourglass filter banks in 2-D, either critically sampled [1]–[4] or nonsubsampled [5], [6]; and in 3-D, but without perfect reconstruction [11], [13]. However, to our best knowledge, studies on hourglass filter banks in 3-D and higher dimensions with perfect reconstruction properties have not been reported until recently. In [10], we proposed a design of multidimensional hourglass filter banks based on frequency domain techniques. The drawback of that design is that the resulting filters do not have rational z-transforms. The filtering operations then have to be implemented in the Fourier domain by first taking the FFT of the input signal and then multiplying it with the frequency values of the filters. In practice, this FFT-based implementation often requires a large memory space (especially in 3-D and higher dimensional cases), and can cause long buffer delays which are undesirable for applications such as video processing.

In this paper, we propose a novel mapping-based design for the hourglass filter banks in arbitrary dimensions, featuring perfect reconstruction, finite impulse response (FIR) filters, efficient implementation using lifting/ladder structures [16], [17], and a near-tight frame construction. Compared with the frequency-domain implementation, the FIR filters allow the filtering operations to be carried out in the spatial domain with only partial input signal available in the memory, a property potentially favorable to real-time applications and hardware implementations.

The outline of the paper is as follows. Section II provides a formal definition of the passband supports of hourglass filter banks in arbitrary dimensions, which serves as the foundation for subsequent discussions. We propose our mapping-based filter bank design in Section III, and study the conditions on suitable passband supports of mapping kernels in Section IV. The goal of these conditions is to ensure that the resulting overall filters still have good frequency responses when the component filters used are nonideal. Since suitable mapping kernels are not unique, we propose an optimal specification for the kernels, which, among all possible choices, leads to the simplest passband shapes and involves the fewest number of frequency variables. The two ingredients of the mapping-based design, i.e., the 1-D polynomials and mapping kernels, are designed in Section V. These designs endow the filter banks with additional properties, including an efficient lifting/ladder-based implementation and a near-tight frame construction. Finally, to illustrate the proposed design scheme, we present a numerical example for the hourglass filter bank in 3-D, and an application in video denoising. We conclude the paper in Section VI.

II. Passband Geometry of Multidimensional Hourglass Filters

A. Notations

Before proceeding, we indicate some notational conventions that will be used in the following. Throughout the paper, d represents the dimension of the filters under consideration. We are interested in cases when $d \geq 2$. We use lower-case letters, such as $x[\boldsymbol{n}]$, to denote d-D discrete filters, where $\boldsymbol{n} = (n_1, n_2, \ldots, n_d)^T$ is an integer vector. Correspondingly, $X(e^{j\boldsymbol{\omega}})$ stands for the Fourier transform of $x[\boldsymbol{n}]$, with $\boldsymbol{\omega} = (\omega_1, \ldots, \omega_d)^T$. We use script letters, e.g., $\mathcal{X}$, to represent the passband supports of filter frequency responses, and denote $\mathbb{1}_{\mathcal{X}}(\boldsymbol{\omega})$ as the indicator function defined on $\mathcal{X}$, i.e., $\mathbb{1}_{\mathcal{X}}(\boldsymbol{\omega}) = 1$ if $\boldsymbol{\omega} \in \mathcal{X}$ and $\mathbb{1}_{\mathcal{X}}(\boldsymbol{\omega}) = 0$ otherwise.

We use $\Lambda \subseteq \{1, 2, \ldots, d\}$ to represent an arbitrary subset of frequency indices, whose cardinality is written as $|\Lambda|$. For any positive real number α, the value $\lfloor \alpha \rfloor$ denotes the largest integer less than or equal to α, while $\lceil \alpha \rceil$ denotes the smallest integer greater than or equal to α.

B. The Passband Supports of Hourglass Filter Banks

The following is a precise definition of the passband supports of the proposed hourglass filter banks in arbitrary d-D cases.

Definition 1: The d-D ($d \geq 2$) nonsubsampled hourglass filter bank consists of d analysis filters $\{H_i(e^{j\boldsymbol{\omega}})\}_{i=1}^{d}$ and d synthesis filters $\{G_i(e^{j\boldsymbol{\omega}})\}_{i=1}^{d}$. The ideal passband supports $\mathcal{H}_i$ and $\mathcal{G}_i$ of the ith analysis/synthesis filter pair, $H_i(e^{j\boldsymbol{\omega}})$ and $G_i(e^{j\boldsymbol{\omega}})$, are

$$\mathcal{H}_i = \mathcal{G}_i \stackrel{\text{def}}{=} \{\boldsymbol{\omega} \in (-\pi, \pi]^d : |\omega_i| = \max_{1 \leq j \leq d} |\omega_j|\} + 2\pi\mathbb{Z}^d. \quad (1)$$

Note that $2\pi\mathbb{Z}^d \stackrel{\text{def}}{=} \{2\pi\boldsymbol{n} : \boldsymbol{n} \in \mathbb{Z}^d\}$ in (1) represents the 2π-periodicity of frequency responses. Since the analysis and synthesis filters have the same passband supports, we will concentrate on the analysis filters in the following discussions.

In the 2-D and 3-D cases, we can easily verify that the definition in (1) indeed specifies the hourglass-shaped passband supports as shown in Fig. 1(a) and (b), respectively. In the general

d-D case, it follows from (1) that the ith filter $H_i(e^{j\boldsymbol{\omega}})$ only selects frequencies that are closer to the ith frequency axis than to any other axis. Therefore, the proposed hourglass filter banks in d-D can decompose the frequency spectrum into d directional subbands, each aligned with one of the frequency axes.

From the definition given in (1), we can easily verify the following result, which will be used in the derivation of our proposed mapping-based filter bank design.

Lemma 1: Let $\Lambda \subseteq \{1, 2, \ldots, d\}$ be a subset of indices and denote $\mathcal{H}_\Lambda$ as the union of all frequency regions $\mathcal{H}_i$ with i drawn from Λ. Then

$$\mathcal{H}_\Lambda \stackrel{\text{def}}{=} \bigcup_{i\in\Lambda} \mathcal{H}_i = \{\boldsymbol{\omega} \in (-\pi, \pi]^d : \max_{i\in\Lambda} |\omega_i| = \max_{1\le j\le d} |\omega_j|\} + 2\pi\mathbb{Z}^d. \quad (2)$$

III. A Mapping-Based Design for the Hourglass Filter Banks

In this section, we deal with the filter design of the multidimensional nonsubsampled hourglass filter banks. The goal is to find a set of FIR filters $\{h_i[\boldsymbol{n}]\}_{i=1}^d$ and $\{g_i[\boldsymbol{n}]\}_{i=1}^d$, such that their frequency responses are good approximations of the ideal hourglass filters as defined in (1), and that, without any subband processing in Fig. 2, the perfect reconstruction condition is satisfied, i.e.

$$\sum_{i=1}^{d} H_i(e^{j\boldsymbol{\omega}})\, G_i(e^{j\boldsymbol{\omega}}) = 1. \quad (3)$$

Thanks to the nonsubsampled structure of the hourglass filter banks, the above condition is much milder than the usual perfect reconstruction conditions required by critically sampled filter banks [18], [19].

A. Design of Two-Channel Nonsubsampled Filter Banks Using Mapping

A common approach to the design of nonseparable multidimensional filters is based on mapping (i.e., transformation of variables) [20]–[22], [2]. Although the mapping approach imposes certain restrictions on the kind of filters we can get, it brings many important advantages, including, as we will demonstrate later, efficient implementation and extendable general design for arbitrary dimensions. These advantages can be especially useful in higher dimensional (e.g., $d \ge 3$) cases.

For the sake of completeness, we briefly explain the basic idea of this mapping approach for the two-channel, nonsubsampled case as follows: first, we design 1-D polynomials $f_1(x)$, $f_2(x)$ (for the analysis part), and $e_1(x)$ $e_2(x)$ (for the synthesis part) that satisfy the Bézout's identity

$$f_1(x)\, e_1(x) + f_2(x)\, e_2(x) = 1. \quad (4)$$

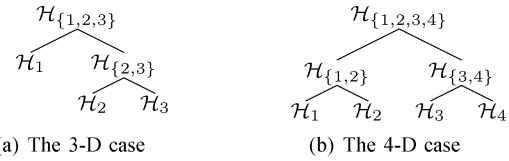

(a) The 3-D case (b) The 4-D case

Fig. 3. Construction of the multichannel hourglass filter banks through a cascade of two-channel mapped filter banks.

Meanwhile, we control the shape of the polynomials so that $f_i(x) \approx e_i(x)$ for $i = 1, 2$, and that

$$f_1(1) \approx f_2(-1) \approx 1, \quad \text{and} \quad f_1(-1) \approx f_2(1) \approx 0. \quad (5)$$

The details of how to find these polynomials will be given in Section V. We refer readers to Fig. 8 for an example of these polynomials.

Next, we find a mapping kernel $K(e^{j\boldsymbol{\omega}})$, which is the Fourier transform of some multidimensional zero phase FIR filter. Now the key step in the mapping-based design is to substitute the variable x in the polynomials with $K(e^{j\boldsymbol{\omega}})$ and define the analysis filters $F_i(e^{j\boldsymbol{\omega}})$ and synthesis filters $E_i(e^{j\boldsymbol{\omega}})$ as

$$F_i(e^{j\boldsymbol{\omega}}) = f_i\left(K(e^{j\boldsymbol{\omega}})\right) \text{ and } E_i(e^{j\boldsymbol{\omega}}) = e_i\left(K(e^{j\boldsymbol{\omega}})\right), \text{ for } i = 1, 2. \quad (6)$$

Several nice properties come from this mapping of variables. First, the Bézout's identity (4) of the 1-D polynomials ensures that the perfect reconstruction condition in (3) (with H_i and G_i replaced by F_i and E_i) is satisfied with arbitrary choices of $K(e^{j\boldsymbol{\omega}})$. Meanwhile, same as the kernel $K(e^{j\boldsymbol{\omega}})$, the resulting multidimensional filters $F_i(e^{j\boldsymbol{\omega}})$ and $E_i(e^{j\boldsymbol{\omega}})$ in (6) are still FIR, and have zero phase.

To control frequency responses, we can design the mapping kernel such that $K(e^{j\boldsymbol{\omega}}) \approx 1$ for $\boldsymbol{\omega} \in \mathcal{K}$ and $K(e^{j\boldsymbol{\omega}}) \approx -1$ for $\boldsymbol{\omega} \in \mathcal{K}^C$, where $\mathcal{K} \subseteq \mathbb{R}^d$ is the desired passband support of the filter bank, and $\mathcal{K}^C$ is the complement of $\mathcal{K}$. It then follows from the shape of the polynomials specified in (5) that the mapped filters in (6) can be written as $F_1(e^{j\boldsymbol{\omega}}) \approx E_1(e^{j\boldsymbol{\omega}}) \approx \mathbb{1}_{\mathcal{K}}$ and $F_2(e^{j\boldsymbol{\omega}}) \approx E_2(e^{j\boldsymbol{\omega}}) \approx \mathbb{1}_{\mathcal{K}^C}$, where $\mathbb{1}_{\mathcal{K}}$ and $\mathbb{1}_{\mathcal{K}^C}$ are the indicator functions on $\mathcal{K}$ and $\mathcal{K}^C$, respectively.

B. Extension to the Multichannel Case

The nonsubsampled hourglass filter banks discussed in this paper have d channels in the general d-D case. To extend the mapping technique to the multichannel cases, we propose to use a cascade of two-channel filter banks.

The idea can be explained by the tree graph in Fig. 3(a) for the 3-D case. Recall from Lemma 1 that the entire 3-D spectrum can be written as the union of all three hourglass-shaped supports $\mathcal{H}_i$, for $i = 1, 2, 3$. Now, starting from the root of the tree, which is denoted as $\mathcal{H}_{\{1,2,3\}}$, we first use a two channel mapped filter bank, with a suitable kernel $K_1(e^{j\boldsymbol{\omega}})$, to divide the spectrum into two parts: $\mathcal{H}_1$ and $\mathcal{H}_{\{2,3\}}$. Leaving the first node alone, we then attach another two-channel mapped filter bank, with a different kernel $K_2(e^{j\boldsymbol{\omega}})$, to further divide $\mathcal{H}_{\{2,3\}}$ into $\mathcal{H}_2$ and $\mathcal{H}_3$.

Assume the polynomials used in the analysis part of the mapped filter banks are $f_1(x)$ and $f_2(x)$, then the resulting analysis filters are

$$\begin{aligned} H_1(e^{j\boldsymbol{\omega}}) &= f_1(K_1(e^{j\boldsymbol{\omega}})) \\ H_2(e^{j\boldsymbol{\omega}}) &= f_2(K_1(e^{j\boldsymbol{\omega}}))\, f_1(K_2(e^{j\boldsymbol{\omega}})) \\ H_3(e^{j\boldsymbol{\omega}}) &= f_2(K_1(e^{j\boldsymbol{\omega}}))\, f_2(K_2(e^{j\boldsymbol{\omega}})) \end{aligned} \tag{7}$$

and the synthesis filters take similar forms. Note that the above strategy can be easily generalized to higher dimensional cases. For example, we show in Fig. 3(b) the cascade structure for the 4-D hourglass filter bank, which decomposes the spectrum into four hourglass subbands, with two levels of decomposition and three different two-channel mapped filter banks. In the general d-D case, the proposed cascade tree for frequency partitioning is built up, in a recursive fashion, as follows.

1) Procedure 1: We start with a tree containing a single node, whose corresponding frequency support is the entire spectrum.

(1) For any leaf node in the current tree, we can write the frequency support of the equivalent filter at that node as a region $\mathcal{H}_\Lambda$ defined in **(2)**. Note that in the beginning, we have $\Lambda = \{1, 2, \ldots, d\}$ and, hence, $\mathcal{H}_\Lambda = \mathbb{R}^d$. Unless Λ is a singleton set (i.e., $|\Lambda| = 1$), we will use a two-channel mapped filter bank to further split the node into two child nodes. The goal is to divide the frequency support $\mathcal{H}_\Lambda$ into two smaller regions $\mathcal{H}_{\Lambda_1}$ and $\mathcal{H}_{\Lambda\setminus\Lambda_1}$, where $\Lambda_1 \subset \Lambda$. To achieve a balanced filter bank, we choose Λ_1 to be the set of the first $\lfloor |\Lambda|/2 \rfloor$ indices in Λ.

(2) Repeat step (1) until all leaf nodes in the tree are supported on the hourglass-shaped regions $\mathcal{H}_i$ for $i = 1, 2, \ldots, d$.

We can easily verify that the above cascade scheme consists of $\lceil \log_2(d) \rceil$ levels of decomposition and uses $d-1$ different two channel filter banks.

There are several advantages in using the proposed cascade scheme. First, it simplifies the problem of designing a d-channel multidimensional filter bank to the more tractable task of designing $d-1$ two-channel mapped filter banks. As long as each two-channel filter bank achieves perfect reconstruction with zero phase FIR filters, the resulting d-channel filter banks also have perfect reconstruction with zero phase FIR filters. Second, as we can see from Fig. 3, filters resulting from the cascade scheme automatically come with a tree-structured factorization. This form of implementation often requires fewer arithmetic operations than a direct parallel implementation of the same filter bank.

IV. Passband Supports of the Mapping Kernels

A. Intuition and Motivation

The cascading scheme described in Procedure 1 can be intuitively interpreted as a "cake-cutting" process. As shown in Fig. 3, the original frequency spectrum — a cube-shaped "cake" — is cut into two pieces at a time by a sequence of two-channel filter banks. One important remaining task in the design is to specify the passband support of each filter bank (i.e., where to make the cut at each step), so that the resulting overall filters indeed achieve the desired hourglass-shaped passband supports.

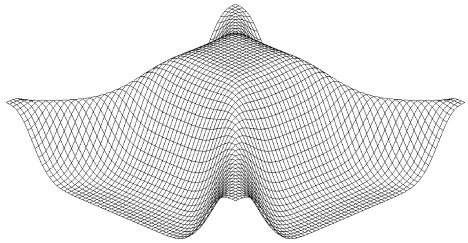

Fig. 4. The 2-D frequency response $H_{3,a}(e^{j(\omega_1,\omega_2,\pi/3)})$ of a 3-D FIR filter designed by using an incorrect mapping kernel.

The 2-D case is simple and straightforward, since we just need to use a single two-channel filter bank, whose frequency support is uniquely determined. However, it becomes more interesting when we construct 3-D and higher dimensions hourglass filter banks.

For example, let us consider the 3-D case with a two-level cascading structure given in Fig. 3(a). As specified by the frequency dividing scheme, in the first level, we use a two-channel mapped filter bank with a mapping kernel supported on $\mathcal{H}_1$. (Recall that $\{\mathcal{H}_i,\ i = 1, 2, 3\}$ represent the hourglass-shaped frequency supports defined in (1).) As a result, we get two filters, whose Fourier transforms can be approximated by $\mathbb{1}_{\mathcal{H}_1}(\boldsymbol{\omega})$ and $\mathbb{1}_{\mathcal{H}_2\cup\mathcal{H}_3}(\boldsymbol{\omega})$, respectively. In the second level of Fig. 3(a), we need to further divide the filter $\mathbb{1}_{\mathcal{H}_2\cup\mathcal{H}_3}(\boldsymbol{\omega})$ by using another two-channel filter bank; and it is at this step that we have more options.

One possible choice is to choose $\mathcal{K}_a \stackrel{\text{def}}{=} \mathcal{H}_2$ as the passband support of the mapping kernel used by the second filter bank. Applied after the filter $\mathbb{1}_{\mathcal{H}_2\cup\mathcal{H}_3}(\boldsymbol{\omega})$ from the previous level, this second filter bank will then generate two equivalent filters as

$$\begin{aligned} H_{2,a}(e^{j\boldsymbol{\omega}}) &\approx \mathbb{1}_{\mathcal{H}_2\cup\mathcal{H}_3}(\boldsymbol{\omega})\, \mathbb{1}_{\mathcal{H}_2}(\boldsymbol{\omega}) = \mathbb{1}_{\mathcal{H}_2}(\boldsymbol{\omega}), \quad \text{and} \\ H_{3,a}(e^{j\boldsymbol{\omega}}) &\approx \mathbb{1}_{\mathcal{H}_2\cup\mathcal{H}_3}(\boldsymbol{\omega})\, \mathbb{1}_{\mathcal{H}_2^C}(\boldsymbol{\omega}) \\ &= \mathbb{1}_{\mathcal{H}_2\cup\mathcal{H}_3}(\boldsymbol{\omega})\, \mathbb{1}_{\mathcal{H}_1\cup\mathcal{H}_3}(\boldsymbol{\omega}) = \mathbb{1}_{\mathcal{H}_3}(\boldsymbol{\omega}). \end{aligned} \tag{8}$$

However, another possible choice is to use

$$\mathcal{K}_b \stackrel{\text{def}}{=} \{\boldsymbol{\omega} \in (-\pi, \pi]^d : |\omega_2| \geq |\omega_3|\} + 2\pi\mathbb{Z}^d \tag{9}$$

as the passband support of the mapping kernel. We will show in Section IV-C that the resulting equivalent filters in this case can also be written as

$$\begin{aligned} H_{2,b}(e^{j\boldsymbol{\omega}}) &\approx \mathbb{1}_{\mathcal{H}_2\cup\mathcal{H}_3}(\boldsymbol{\omega})\, \mathbb{1}_{\mathcal{K}_b}(\boldsymbol{\omega}) = \mathbb{1}_{\mathcal{H}_2}(\boldsymbol{\omega}) \quad \text{and} \\ H_{3,b}(e^{j\boldsymbol{\omega}}) &\approx \mathbb{1}_{\mathcal{H}_2\cup\mathcal{H}_3}(\boldsymbol{\omega})\, \mathbb{1}_{\mathcal{K}_b^C}(\boldsymbol{\omega}) = \mathbb{1}_{\mathcal{H}_3}(\boldsymbol{\omega}). \end{aligned} \tag{10}$$

From (8) and (10), it seems that both $\mathcal{K}_a$ or $\mathcal{K}_b$ can lead to filters that are "approximately" supported on the hourglass-shaped supports $\mathcal{H}_2$ and $\mathcal{H}_3$, and, hence, either one of them can be used as the passband support of the second mapped filter bank. However, this is true only when all the filters are ideal; in fact, the two choices make a big difference in practice, when we use nonideal filters.

For example, Fig. 4 shows a 2-D slice of the 3-D frequency response $H_{3,a}(e^{j\boldsymbol{\omega}})$ of an FIR filter, designed by using the first

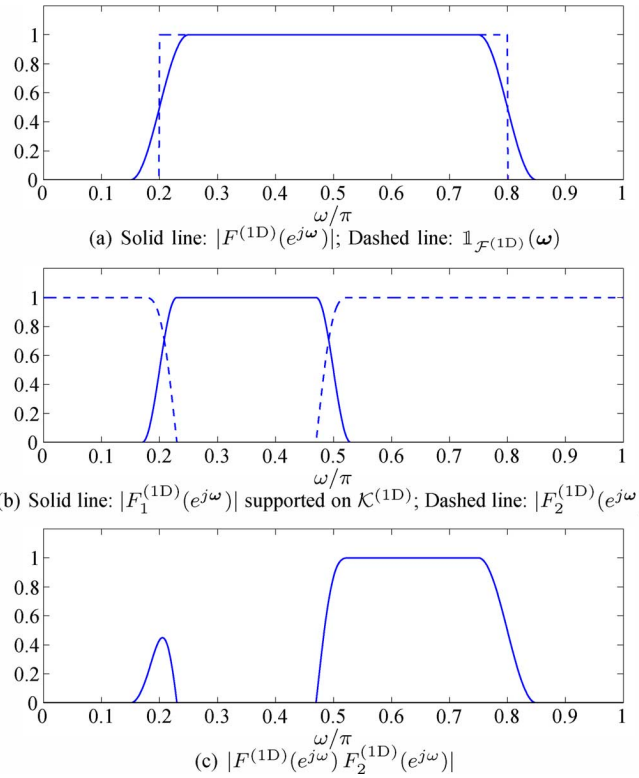

Fig. 5. Illustration of problems when the frequency support of the mapping kernel is not chosen appropriately.

choice $\mathcal{K}_a$. Notice that the 2-D slice, taken at $\omega_3 = \pi/3$, are supposed to display a lowpass response. However, we can see from the figure that the actual 2-D response contains lots of undesirable out-of-band energy. In sharp contrast, we will show both analytically (see Section IV-C) and by numerical examples (see Fig. 9) that $\mathcal{K}_b$, the second choice for the passband support, can lead to FIR filters with much better frequency localization.

For easy visualization, we explain the above problem by an analogous 1-D example illustrated in Fig. 5. Let $F^{(1D)}(e^{j\omega})$ (shown in solid lines in Fig. 5(a)) be a 1-D filter approximating the ideal indicator function $\mathbb{1}_{[0.2\pi,0.8\pi]}$ (shown in dashed lines). Analogous to the situation in our cascaded hourglass filter banks, we want to use a two-channel mapped filter bank to decompose the original passband ($\mathcal{F}^{(1D)} = [0.2\pi, 0.8\pi]$) into $\mathcal{F}_1^{(1D)} = [0.2\pi, 0.5\pi]$ and $\mathcal{F}_2^{(1D)} = [0.5\pi, 0.8\pi]$. Now suppose the passband support of the mapping kernel is chosen to be $\mathcal{K}^{(1D)} = [0.2\pi, 0.5\pi]$. We plot in Fig. 5(b) the two component filters $F_1^{(1D)}(e^{j\omega})$ and $F_2^{(1D)}(e^{j\omega})$ resulting from this mapping kernel, and in Fig. 5(c) one of the equivalent filters $F^{1D}(e^{j\omega})\,F_2^{1D}(e^{j\omega})$ obtained after applying the mapped filter bank. We can see from Fig. 5(c) that, although most of the subband energy is concentrated on the desired passband $[0.5\pi, 0.8\pi]$, there is a large bump at 0.2π. We can reduce the width of the bump by employing sharper filters. However, as long as the filter responses are not ideal indicator functions, the magnitude of the bump can not be reduced. On the other hand, if we change the support of the mapping kernel to $\mathcal{K}^{(1D)} = [c, 0.5\pi]$ for any $0 \le c \le 0.1\pi$, then the resulting filter responses will not contain any undesirable bump.

The above discussions on 3-D and 1-D examples offer two important insights: first, in searching for suitable mapping kernel supports, we cannot use the (overly) simplified indicator functions to model the frequency responses of practical filters; second, suitable mapping kernels are not unique (see the 1-D example). Consequently, there is also the problem of picking the "optimal" one among all suitable choices. We address the first issue in Section IV-B and propose solutions to the second problem in Section IV-C, both for the general d-D ($d \ge 2$) cases. In particular, we will show that the mapping kernel $\mathcal{K}_b$ defined in (9) is the optimal choice in the 3-D case.

B. General Conditions for the Passband Supports of Mapping Kernels

In this section, we derive the general conditions for mapping kernels, under which we can still get good frequency responses when the component filters used are nonideal. Complementary to the previous geometrical intuitions, we introduce and employ some additional algebraic notations here. These notations not only provide a more rigorous ground for our derivation, but more importantly, allow us to obtain general results that are valid for arbitrary dimensional cases.

As shown in Fig. 3, we can associate any node in the proposed cascade filter bank tree with an index set Λ. For example, for the node denoted by $\mathcal{H}_{\{3,4\}}$ in Fig. 3(b), we have $\Lambda = \{3, 4\}$. The equivalent filter $F_\Lambda(e^{j\boldsymbol{\omega}})$ at node Λ is obtained as the product of all filters along the path from the root leading to that node. Denote $\mathcal{F}_\Lambda$ as the ideal passband support of $F_\Lambda(e^{j\boldsymbol{\omega}})$, then according to Procedure 1 , our design requires that

$$\mathcal{F}_\Lambda = \mathcal{H}_\Lambda = \bigcup_{i \in \Lambda} \mathcal{H}_i. \tag{11}$$

If the node Λ is not at the bottom of the tree, we then subsequently decompose $F_\Lambda(e^{j\boldsymbol{\omega}})$ by a two-channel mapped filter bank with a mapping kernel $K(e^{j\boldsymbol{\omega}})$, and generate two equivalent filters for the two child nodes Λ_1 and $\Lambda \setminus \Lambda_1$ at the next level as

$$F_{\Lambda_1}(e^{j\boldsymbol{\omega}}) = F_\Lambda(e^{j\boldsymbol{\omega}})\,F_1(e^{j\boldsymbol{\omega}}) \tag{12}$$

and

$$F_{\Lambda\setminus\Lambda_1}(e^{j\boldsymbol{\omega}}) = F_\Lambda(e^{j\boldsymbol{\omega}})\,F_2(e^{j\boldsymbol{\omega}}) \tag{13}$$

where Λ_1 is a subset of Λ as chosen in Procedure 1 ; F_1 and F_2 are the two component filters of the two-channel mapped filter bank defined in (6). As shown in Section III-A, if $\mathcal{K}$ is the ideal passband support of the mapping kernel $K(e^{j\boldsymbol{\omega}})$, then the component filters satisfy $F_1(e^{j\boldsymbol{\omega}}) \approx \mathbb{1}_{\mathcal{K}}(\boldsymbol{\omega})$ and $F_2(e^{j\boldsymbol{\omega}}) \approx \mathbb{1}_{\mathcal{K}^C}(\boldsymbol{\omega})$.

Our question now becomes: how do we choose $\mathcal{K}$ so that the two resulting equivalent filters F_{Λ_1} and $F_{\Lambda\setminus\Lambda_1}$ in (12) and (13) achieve the required passband supports

$$\mathcal{F}_{\Lambda_1} = \mathcal{H}_{\Lambda_1} \quad \text{and} \quad \mathcal{F}_{\Lambda\setminus\Lambda_1} = \mathcal{H}_{\Lambda\setminus\Lambda_1} \tag{14}$$

respectively?

The answer would be straightforward if all filters are ideal indicator functions on their passbands: we can simply choose

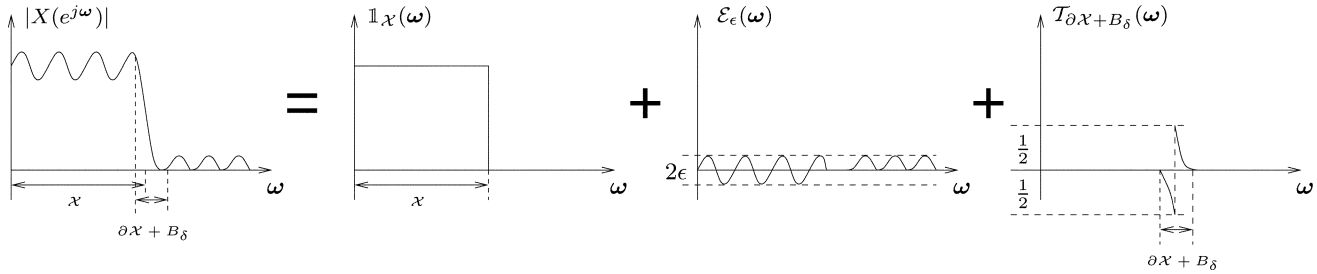

Fig. 6. Decomposition of the magnitude response $|X(e^{j\boldsymbol{\omega}})|$ as the sum of the indicator function $\mathbb{1}_{\mathcal{X}}(\boldsymbol{\omega})$, the in-band ripple term $\mathcal{E}_\epsilon(\boldsymbol{\omega})$, and the bump function $\mathcal{T}_{\partial\mathcal{X}+B_\delta}(\boldsymbol{\omega})$ at the transition band.

$\mathcal{K} = \mathcal{H}_{\Lambda_1}$, and verify (14) by substituting each filter in (12) and (13) with the corresponding indicator function. However, we know from previous discussions that this simple solution will lead to problems in practice, when we use nonideal filters.

Given the magnitude frequency response $|X(e^{j\boldsymbol{\omega}})|$ of a filter, we use two numbers ϵ and δ to measure how close $|X(e^{j\boldsymbol{\omega}})|$ is to the indicator function $\mathbb{1}_{\mathcal{X}}(\boldsymbol{\omega})$ as follows:

$$\sup_{\boldsymbol{\omega}\notin\partial\mathcal{X}+B_\delta} \Big||X(e^{j\boldsymbol{\omega}})| - \mathbb{1}_{\mathcal{X}}(\boldsymbol{\omega})\Big| \le \epsilon \tag{15}$$

where $\partial\mathcal{X}$ is the set of boundary points of the passband support $\mathcal{X}$, and $B_\delta \stackrel{\text{def}}{=} \{\boldsymbol{\omega} : \|\boldsymbol{\omega}\| \le \delta\}$ is the d-D ball of radius δ. For example, if $\mathcal{X}$ is the 2-D hourglass-shaped support shown in Fig. 1(a), then its boundary $\partial\mathcal{X}$ consists of the two diagonal lines $\omega_1 = \pm\omega_2$. Note that in (15), ϵ characterizes the maximum variation (i.e., ripple) of the frequency response in the passband and stopband; while δ measures the width of the transition band $\partial\mathcal{X} + B_\delta$.

As illustrated in Fig. 6 for the 1-D case, we can rewrite $|X(e^{j\boldsymbol{\omega}})|$ satisfying (15) as

$$|X(e^{j\boldsymbol{\omega}})| = \mathbb{1}_{\mathcal{X}}(\boldsymbol{\omega}) + \mathcal{E}_\epsilon(\boldsymbol{\omega}) + \mathcal{T}_{\partial\mathcal{X}+B_\delta}(\boldsymbol{\omega}) \tag{16}$$

where $\mathcal{E}_\epsilon(\boldsymbol{\omega})$ belongs to a class of functions whose maximum absolute values are less than ϵ; $\mathcal{T}_{\partial\mathcal{X}+B_\delta}$ belongs to a class of bump functions supported on the transition band and defined as

$$\Big\{f(\boldsymbol{\omega}) : \operatorname{supp}(f) \subseteq \partial\mathcal{X} + B_\delta \text{ and } |f(\boldsymbol{\omega})| = \frac{1}{2} \text{ for } \boldsymbol{\omega} \in \partial\mathcal{X}\Big\}.$$

It is to be noted that, instead of being some exact functions, the terms $\mathcal{E}_\epsilon(\boldsymbol{\omega})$ and $\mathcal{T}_{\partial\mathcal{X}+B_\delta}$ in (16) should be interpreted as instances from two classes of functions, which are used to characterize the in-band ripple and the transition band of $|X(e^{j\boldsymbol{\omega}})|$, respectively.

Applying the notation introduced in (16), we can rewrite the zero phase equivalent filter at node Λ as $F_\Lambda(e^{j\boldsymbol{\omega}}) = \mathbb{1}_{\mathcal{H}_\Lambda}(\boldsymbol{\omega}) + \mathcal{E}_\epsilon(\boldsymbol{\omega}) + \mathcal{T}_{\partial\mathcal{H}_\Lambda+B_\delta}(\boldsymbol{\omega})$; and the two component filters from the two-channel mapped filter bank as $F_1(e^{j\boldsymbol{\omega}}) = \mathbb{1}_{\mathcal{K}}(\boldsymbol{\omega}) + \mathcal{E}_\epsilon(\boldsymbol{\omega}) + \mathcal{T}_{\partial\mathcal{K}+B_\delta}(\boldsymbol{\omega})$ and $F_2(e^{j\boldsymbol{\omega}}) = \mathbb{1}_{\mathcal{K}^C}(\boldsymbol{\omega}) + \mathcal{E}_\epsilon(\boldsymbol{\omega}) + \mathcal{T}_{\partial\mathcal{K}^C+B_\delta}(\boldsymbol{\omega})$, respectively. For simplicity of notation, we use the same parameters ϵ and δ for all three filters.

Lemma 2: For small values of ϵ and δ, the zero phase equivalent filters at nodes Λ_1 and $\Lambda \setminus \Lambda_1$ as defined in (12) and (13) can be written as

$$F_{\Lambda_1}(e^{j\boldsymbol{\omega}}) \approx \mathbb{1}_{\mathcal{H}_\Lambda\cap\mathcal{K}}(\boldsymbol{\omega}) + 2\,\mathcal{E}_\epsilon(\boldsymbol{\omega}) + \mathcal{T}_{\partial(\mathcal{H}_\Lambda\cap\mathcal{K})+B_\delta}(\boldsymbol{\omega}) + \frac{1}{2}\,\mathcal{T}_{\partial\mathcal{H}_\Lambda\cap\partial\mathcal{K}+B_\delta}(\boldsymbol{\omega}) \tag{17}$$

and

$$F_{\Lambda\setminus\Lambda_1}(e^{j\boldsymbol{\omega}}) \approx \mathbb{1}_{\mathcal{H}_\Lambda\cap\mathcal{K}^C}(\boldsymbol{\omega}) + 2\,\mathcal{E}_\epsilon(\boldsymbol{\omega}) + \mathcal{T}_{\partial(\mathcal{H}_\Lambda\cap\mathcal{K}^C)+B_\delta}(\boldsymbol{\omega}) + \frac{1}{2}\,\mathcal{T}_{\partial\mathcal{H}_\Lambda\cap\partial\mathcal{K}+B_\delta}(\boldsymbol{\omega}). \tag{18}$$

Proof: See Appendix A. ■

Recall from (14) that our goal is to have $F_{\Lambda_1}(e^{j\boldsymbol{\omega}}) \approx \mathbb{1}_{\mathcal{H}_{\Lambda_1}}(\boldsymbol{\omega})$ and $F_{\Lambda\setminus\Lambda_1}(e^{j\boldsymbol{\omega}}) \approx \mathbb{1}_{\mathcal{H}_{\Lambda\setminus\Lambda_1}}(\boldsymbol{\omega})$. It follows immediately from (17) that we need $\mathcal{H}_\Lambda \cap \mathcal{K} = \mathcal{H}_{\Lambda_1}$, which then also guarantees that $\mathcal{H}_\Lambda \cap \mathcal{K}^C = \mathcal{H}_{\Lambda\setminus\Lambda_1}$. Next, we observe that there are two terms in (17) related to the transition band of the frequency response. However, we know that the transition can only happen at the boundary of the desired passband $\mathcal{H}_\Lambda \cap \mathcal{K}$, since otherwise the frequency response would contain an out-of-band bump [e.g., see Fig. 5(c)]. Therefore, we must have $\partial\mathcal{H}_\Lambda \cap \partial\mathcal{K} \subseteq \partial(\mathcal{H}_\Lambda \cap \mathcal{K}) = \partial\mathcal{H}_{\Lambda_1}$. Based on the same reasoning, we can derive from (18) that $\partial\mathcal{H}_\Lambda \cap \partial\mathcal{K} \subseteq \partial(\mathcal{H}_\Lambda \cap \mathcal{K}^C) = \partial\mathcal{H}_{\Lambda\setminus\Lambda_1}$. In summary, we reach the following design requirements:

Condition 1: For the two filters $F_{\Lambda_1}(e^{j\boldsymbol{\omega}})$ and $F_{\Lambda\setminus\Lambda_1}(e^{j\boldsymbol{\omega}})$ to be well localized on their desired passband regions, the passband support $\mathcal{K}$ of the mapping kernel must satisfy the following two conditions:

$$\mathcal{H}_\Lambda \cap \mathcal{K} = \mathcal{H}_{\Lambda_1}, \qquad \text{and} \tag{19}$$

$$\partial\mathcal{H}_\Lambda \cap \partial\mathcal{K} \subseteq \partial\mathcal{H}_{\Lambda_1} \cap \partial\mathcal{H}_{\Lambda\setminus\Lambda_1} \tag{20}$$

where $\mathcal{H}_\Lambda$, $\mathcal{H}_{\Lambda_1}$, and $\mathcal{H}_{\Lambda\setminus\Lambda_1}$ are the frequency regions defined in (2).

Intuitively, the equality in (19) implies that $\mathcal{K}$ "cuts" $\mathcal{H}_{\Lambda_1}$ out of $\mathcal{H}_\Lambda$; the boundary condition given in (20) further requires that the "cut" should only happen at the location where the boundaries of $\mathcal{H}_{\Lambda_1}$ and $\mathcal{H}_{\Lambda\setminus\Lambda_1}$ intersect. The purpose of condition (20) is to ensure that the resulting frequency responses will be free of out-of-band bumps even if the component filters used in the design are nonideal. For example, we can verify that the kernel $\mathcal{K}^{(1D)}$ shown in Fig. 5(b) only satisfies (19) but not (20) (after replacing $\mathcal{H}_\Lambda$ and $\mathcal{H}_{\Lambda_1}$ with their respective 1-D counterparts $\mathcal{F}^{(1D)}$ and $\mathcal{F}_1^{(1D)}$); consequently, one of the resulting filters contains an undesirable bump in Fig. 5(c).

C. The Simplest Constructions of the Passband Supports

Condition 1 provides the general characterization for the passband supports of all mapping kernels that can be used in our design. However, as we learn from the 1-D example shown in Fig. 5, suitable mapping kernels for a given problem are generally not unique. In the following, we propose a particular

class of kernel passband supports, which not only satisfy both design requirements in Condition 1 but also have the simplest shapes among all possible choices.

Let Λ be a node in the cascade tree of the hourglass filter banks. To decompose Λ into its child nodes Λ_1 and $\Lambda \setminus \Lambda_1$, we use a two-channel mapped filter bank, whose mapping kernel is supported on

$$\mathcal{K}_{\Lambda,\Lambda_1} = \{\boldsymbol{\omega} \in (-\pi,\pi]^d : \max_{i\in\Lambda_1} |\omega_i| = \max_{j\in\Lambda} |\omega_j|\} + 2\pi\mathbb{Z}^d. \tag{21}$$

Proposition 1: $\mathcal{K}_{\lambda,\lambda_1}$ satisfies the two design requirements given in (19) and (20). Moreover, suppose $\mathcal{K}$ is another passband support that satisfies (19) and (20), then for any boundary facet $\mathcal{B}$ of $\mathcal{K}_{\Lambda,\Lambda_1}$,

$$\emptyset \neq \mathcal{B} \cap \mathcal{H}_\Lambda \subseteq \partial\mathcal{K}. \tag{22}$$

Proof: See Appendix B. ∎

Despite being a d-dimensional region, the passband support $\mathcal{K}_{\Lambda,\Lambda_1}$ defined above can be fully specified by only $|\Lambda|$ frequency variables $\{\omega_i\}_{i\in\Lambda}$. Therefore, in terms of implementation, we only need to design a $|\Lambda|$-dimensional filter (with $|\Lambda| \leq d$) to achieve the passband $\mathcal{K}_{\Lambda,\Lambda_1}$. For example, in the 4-D case shown in Fig. 3(b), we need to use three different two-channel filter banks to split the cascade tree. However, only the one in the first level of decomposition is a 4-D filter bank; the other two used in the second level are both 2-D filter banks, operating on the (ω_1,ω_2) and (ω_3,ω_4) signal planes, respectively.

Furthermore, for any other suitable passband support $\mathcal{K}$, the expression in (22) states that a nonempty portion of any boundary facet of $\mathcal{K}_{\Lambda,\Lambda_1}$ must also belongs to the boundary of $\mathcal{K}$. It then follows that $\mathcal{K}$ must have at least the same number of boundary facets as $\mathcal{K}_{\Lambda,\Lambda_1}$ and consequently involves at least the same number of frequency variables. In other words, $\mathcal{K}_{\Lambda,\Lambda_1}$ has the simplest shape among all possible choices and can be represented by the fewest number of frequency variables. In this sense, the proposed passband support $\mathcal{K}_{\Lambda,\Lambda_1}$ is the optimal solution to our design requirements.

As an application of Proposition 1, we can now establish the optimality of the passband support $\mathcal{K}_b$ given in (9), by realizing that it is just a special 3-D case of $\mathcal{K}_{\Lambda,\Lambda_1}$ with $d=3, \Lambda=\{2,3\}$, and $\Lambda_1=\{2\}$.

V. 1-D Polynomials, Mapping Kernels, and Design Examples

In principle, the mapping-based design method proposed in Section III works for any combination of 1-D polynomials and multidimensional mapping kernels, as long as they satisfy the conditions given in (4), (5), and (21), respectively. In this section, we describe several special choices of the polynomials and kernels that offer some additional desirable properties.

A. 1-D Polynomials Built From Monomial Lifting/Ladder Stages

The Bézout (i.e., perfect reconstruction) condition given in (4) implies that the two polynomials $f_1(x)$ and $f_2(x)$ in the analysis part are coprime, and, hence, we can always factor $f_1(x)$ and $f_2(x)$ into lifting/ladder structures [16], [17] by using the Euclidean algorithm. In our design, we take one step further by imposing the prediction and update filters in the lifting/ladder structures to be monomials, i.e., we let

$$\begin{bmatrix} f_1(x) \\ f_2(x) \end{bmatrix} = \begin{bmatrix} 1 & 0 \\ c_n \cdot x & 1 \end{bmatrix} \times \begin{bmatrix} 1 & c_{n-1}\cdot x \\ 0 & 1 \end{bmatrix} \cdots \times \begin{bmatrix} 1 & 0 \\ c_2 \cdot x & 1 \end{bmatrix} \times \begin{bmatrix} 1 & c_1 \cdot x \\ 0 & 1 \end{bmatrix} \times \begin{bmatrix} k \\ \frac{1}{2k} \end{bmatrix} \tag{23}$$

where k and $c_1,\ldots,c_n$ are free parameters. A similar form of factorization was used by Cunha *et al.* [6] in the design of the 2-D nonsubsampled contourlet transform.

For oversampled filter banks with perfect reconstruction, the synthesis part for a given analysis part is not uniquely determined. In particular, adapting a general result in [23, Theorem 4.1], we can show that all synthesis polynomials $e_1(x)$ and $e_2(x)$ providing perfect reconstruction for the analysis polynomials given in (23) can be written as

$$\begin{bmatrix} e_1(x) \\ e_2(x) \end{bmatrix} = \begin{bmatrix} 1 & -c_n\,x \\ 0 & 1 \end{bmatrix} \times \begin{bmatrix} 1 & 0 \\ -c_{n-1}\,x & 1 \end{bmatrix} \cdots \times \begin{bmatrix} 1 & -c_2\,x \\ 0 & 1 \end{bmatrix} \times \begin{bmatrix} 1 & 0 \\ -c_1\,x & 1 \end{bmatrix} \times \begin{bmatrix} \frac{1+u(x)}{2k} \\ k\,(1-u(x)) \end{bmatrix} \tag{24}$$

where $u(x)$ is an arbitrary polynomial. In our design, we use a particular pair of synthesis polynomials by setting $u(x)\equiv 0$. We can check from (23) and (24) that, for this special case

$$\begin{bmatrix} f_2(-x) \\ f_1(-x) \end{bmatrix} = \begin{bmatrix} 0 & 1 \\ 1 & 0 \end{bmatrix} \begin{bmatrix} f_1(-x) \\ f_2(-x) \end{bmatrix} = \begin{bmatrix} e_1(x) \\ e_2(x) \end{bmatrix}.$$

Since $e_1(x) = f_2(-x)$ and $e_2(x) = f_1(-x)$, the frequency responses in the synthesis part are now complementary to those in the analysis part; consequently, we then just need to design the two analysis polynomials $f_1(x)$ and $f_2(x)$ to achieve the desired shapes.

An important advantage in using the factorization in (23) and (24) is computational efficiency. Recall that in our mapping based design, multidimensional filters are obtained by replacing x in 1-D polynomials with multidimensional mapping kernels $K(e^{j\boldsymbol{\omega}})$. From (23) and (24) (with $u(x)\equiv 0$), any two-channel stage of the multidimensional filter bank can be implemented by a lifting/ladder structure shown in Fig. 7. Note that we actually depict a more generalized form of mapping in the figure, where each lifting/ladder stage can employ a different mapping kernel $K_i(e^{j\boldsymbol{\omega}})$ (for $i=1\ldots n$), and, hence, allowing for more design flexibility. Perfect reconstruction is still achieved in this case, since each lifting/ladder stage in the analysis part can be independently inverted by the corresponding stage in the synthesis part. Compared with direct implementation, the scheme in Fig. 7 can substantially reduce the number of arithmetic operations. We can easily verify the following result.

Proposition 2: Suppose n is the number of lifting stages in (23), d is the dimension of the filter bank, and all the kernels $K_i(e^{j\boldsymbol{\omega}})$ (for $i = 1\ldots n$) are d-D filters of size $\underbrace{m\times m\times\cdots\times m}_{d}$. The lifting/ladder implementation shown in Fig. 7 requires $\mathcal{O}(nm^d)$ arithmetic operations per input sample; while a direct implementation of the same filter bank requires $\mathcal{O}(n^d(m-1)^d)$ arithmetic operations per input sample.

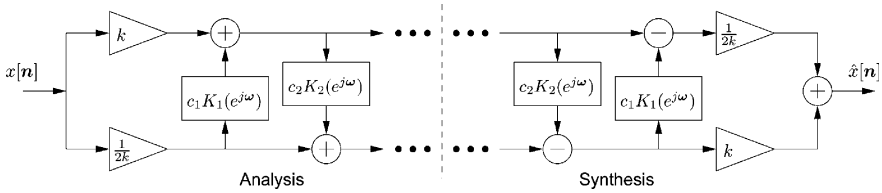

Fig. 7. The lifting/ladder implementation of a two-channel mapped filter bank, whose analysis and synthesis parts are specified by (23) and (24) (with $u(x) \equiv 0$), respectively. Note that we can use a different mapping kernel at each lifting/ladder stage.

We can see that the improvement in computational efficiency becomes more significant, when we work with higher dimensional signals, i.e., when the dimensionality d increases.

To satisfy the shape requirement (5) for 1-D polynomials, we impose the constraints that $f_1(-1) = f_2(1) = 0$ and $f_1(1) = 1$. Note that $f_2(-1) = 1$ is then automatically guaranteed by the perfect reconstruction condition. Under these constraints, we can write k, c_1 and c_2 as functions of the other parameters. For example, when $n = 4$, we have

$$k = \frac{1 + c_3 + c_3 c_4}{2}, \quad c_1 = \frac{(1 + c_3 c_4)^2 - c_3^2}{2} \tag{25}$$

and

$$c_2 = \frac{-1 - c_4}{1 + c_3 + c_3 c_4}. \tag{26}$$

As discussed later the remaining degrees of freedom from c_3 and c_4 can then be explored to endow additional properties to the filter bank.

B. Hourglass Filter Banks as Near-Tight Frames

The connection between nonsubsampled filter banks with the frame expansion of signals has been extensively studied in the past. Here we first briefly recall several appropriate results, and then propose a simple design criterion to make sure the resulting hourglass filter banks are approximately tight frames. Readers unfamiliar with the frame theory in the context of oversampled filter banks are referred to [23], [24], and the references within for more details.

If a nonsubsampled filter bank achieves perfect reconstruction, then its analysis and synthesis parts implement a frame decomposition and a frame reconstruction, respectively. The lower and upper frame bounds for the decomposition frame, denoted by A_E and B_E, can be calculated as [23], [24]

$$A_E = \inf_{\boldsymbol{\omega}} \sum_{i=1}^{d} |H_i(e^{j\boldsymbol{\omega}})|^2 \quad \text{and} \quad B_E = \sup_{\boldsymbol{\omega}} \sum_{i=1}^{d} |H_i(\boldsymbol{\omega})|^2 \tag{27}$$

where $\{H_i(e^{j\boldsymbol{\omega}})\}$ are the d analysis filters. Similarly, the frame bounds A_R and B_R for the reconstruction frame can be calculated by replacing $H_i(e^{j\boldsymbol{\omega}})$ in the above equations with the synthesis filters $G_i(e^{j\boldsymbol{\omega}})$.

The frames become *tight* when $B_E/A_E = B_R/A_R = 1$, which is equivalent to requiring that the analysis filters be power complementary, i.e., $\sum_{i=1}^{d} |H_i(\boldsymbol{\omega})|^2 = \text{const}$. Due to their optimality in noise reduction as well as numerical stability in reconstruction [24], [25], tight frames are often desirable in many applications. However, similar to the classical result on 1-D linear phase filters [18, p. 338], we can also show that the power complementary constraint cannot be met by multidimensional zero phase FIR filters, except for some trivial choices. Now since the resulting hourglass filters from our mapping-based design are always FIR with zero phase, we can only try to approximate the tight frame condition, by making $B_E/A_E \approx B_R/A_R \approx 1$.

However, directly working with B_E/A_E and B_R/A_R can be difficult, since by (27) and (7), these ratios involve both the 1-D polynomials and the specific mapping kernels we use. In our design, we propose to minimize a simple upper bound of the ratios, which only depends on the 1-D polynomials. This choice is justified by the following result, whose proof is given in Appendix C.

Proposition 3: Suppose the 1-D polynomials used in the design are chosen such that $e_1(x) = f_2(-x)$ and $e_2(x) = f_1(-x)$. Meanwhile, suppose $\sup_{\boldsymbol{\omega}} |K(e^{j\boldsymbol{\omega}})| \le 1$ holds for all mapping kernels $K(e^{j\boldsymbol{\omega}})$. The frame bounds of the resulting d-D hourglass filter bank satisfy

$$1 \le \sqrt{\frac{B_E}{A_E}\frac{B_R}{A_R}} \le \left(\max_{|x| \le 1} \left(f_1^2(x) + f_2^2(x) \right) \right)^{2\lceil \log_2(d) \rceil}.$$

Remark 1: By designing the 1-D polynomials to make the quantity $\max_{|x| \le 1} \left(f_1^2(x) + f_2^2(x) \right)$ close to 1, we can effectively "sandwich" the ratios of the frame bounds. As a result, we have $A_E \approx B_E$ and $A_R \approx B_R$, and, hence, the resulting frames are close to being tight. Meanwhile, the assumption that $\sup_{\boldsymbol{\omega}} |K(e^{j\boldsymbol{\omega}})| \le 1$ is always satisfied by mapping kernels designed in Section V-C based on Bernstein polynomials.

Following the above design criterion and applying the relations given in (25) and (26), we then just need to solve an unconstrained nonlinear optimization problem

$$\operatorname*{argmin}_{c_3, c_4} \max_{|x| \le 1} \left(f_1^2(x) + f_2^2(x) \right)$$

with two free variables. Table I shows the optimized parameters $c_1, \ldots, c_4$ and K (obtained using the MATLAB optimization toolbox) and the corresponding maximum values of $f_1^2(x) + f_2^2(x)$ for $|x| \le 1$. Meanwhile, we also show the actual values of the frame bound ratios B_E/A_E and B_R/A_R, computed by (27), of two 3-D hourglass filter banks built from the reported 1-D polynomials. We can see that the frame bound ratios are fairly close to 1, and, hence, the designed filter banks are close to being tight frames.

In principle, we can make the frame bound ratios arbitrarily close to 1 by increasing the number of lifting/ladder stages n, or equivalently the degrees of the polynomials $f_1(x)$ and $f_2(x)$. However, through mapping, this will in turn increase the spatial

TABLE I
THE DESIGNED LIFTING/LADDER COEFFICIENTS ACHIEVING NEAR-TIGHT FRAME CONSTRUCTIONS

n	k	c_1	c_2	c_3	c_4	$\max_{\lvert x\rvert\le 1}\left(f_1^2(x)+f_2^2(x)\right)$	$\frac{B_E}{A_E}$	$\frac{B_R}{A_R}$
3	0.658454	0.449785	−0.759355	0.316907		1.0109	1.018	1.021
4	0.696635	0.276516	−0.566602	0.498169	−0.210571	1.0008	1.003	1.002

TABLE II
3-D BERNSTEIN POLYNOMIALS OF THE FIRST AND SECOND ORDER USED IN THE DESIGN OF MAPPING KERNELS

N	$B(p\,;x_1,x_2,x_3)$
1	$-x_3+x_2x_3-x_2+x_1$
2	$2x_1^2x_2x_3^2+2x_1x_2^2x_3^2+2x_1^2x_2^2x_3-4x_1^2x_2x_3-2x_1^2x_2^2x_3^2+2x_1-2x_2-2x_3+x_3^2+x_2^2-x_1^2$ $+2x_1^2x_2-2x_1x_2^2+4x_2x_3-2x_2^2x_3+2x_1^2x_3-2x_2x_3^2+x_2^2x_3^2-2x_1x_3^2$

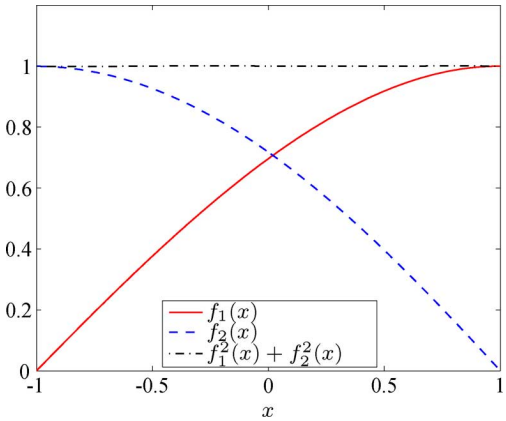

Fig. 8. Designed 1-D polynomials $f_1(x)$ and $f_2(x)$ which lead to near tight frames.

support sizes of the resulting multidimensional filters. In practice, we usually prefer filters that are more compactly supported in space, and, hence, a practical constraint in our design is that we can only use a small number of lifting/ladder stages.

Fig. 8 shows the polynomials $f_1(x)$ and $f_2(x)$ for $n=4$ with their parameters taken from Table I. We can see that $f_1(x)$ is approximately a reversed version of $f_2(x)$, i.e., $f_1(x)\approx f_2(-x)$. Since the synthesis polynomials are defined as $e_1(x)=f_2(-x)$ and $e_2(x)=f_1(-x)$, it then follows that $f_i(x)\approx e_i(x)$ for $i=1,2$, i.e., the analysis and synthesis filters are approximately equal to each other. In other words, the designed filter bank is approximately self-inverting.

C. Mapping Kernels Based on Multivariate Bernstein Polynomials

As shown in Section IV-C, we need to design FIR mapping kernels achieving the passband supports given in (21). For simplicity of exposition, we only consider kernels with the following support regions:

$$\mathcal{K}_{n,m}=\{\boldsymbol{\omega}\in(-\pi,\pi]^d:\max_{i\le m}|\omega_i|=\max_{j\le n}|\omega_j|\}+2\pi\mathbb{Z}^d \quad (28)$$

for some integers m and n with $1\le m<n\le d$. Note that the general kernels with supports defined in (21) can always be obtained from (28) through a change of variables.

There can be several ways to construct the FIR kernels with supports regions approximating (28). One choice is to use an FFT-based iterative design procedure proposed by Cetin and Ansari [26], [27], which leads to approximately equiripple frequency responses. In our design, we choose to use an approach based on multivariate Bernstein polynomials [28]–[30], mainly due to its simplicity provided by the available closed-form solutions.

The general Nth-order Bernstein polynomials with n variables are defined as [31, p. 122]

$$B(p\,;x_1,x_2,\ldots,x_n)=\sum_{k_1=0}^{N}\sum_{k_2=0}^{N}\cdots\sum_{k_n=0}^{N}p\left(\frac{k_1}{N},\frac{k_2}{N},\ldots,\frac{k_n}{N}\right)\times\prod_{i=1}^{n}\binom{N}{k_i}x_i^{k_i}(1-x_i)^{N-k_i} \quad (29)$$

where the polynomial coefficients $p(k_1/N,\ldots,k_n/N)$ are the sample values of a continuous function $p(x_1,\ldots,x_n)$ supported on the unit cube $[0,1]^n$. By making the following change of variables, $x_i\rightarrow\sin^2(\omega_i/2)$ (or equivalently $x_i\rightarrow -(1/4)z_i(1-z_i^{-1})^2$ in the z-domain), we can convert the polynomial $B(p\,;x_1,x_2,\ldots,x_n)$ in (29) into a zero phase FIR filter $K(e^{j\boldsymbol{\omega}})$ with support size $\underbrace{(2N+1)\times\cdots\times(2N+1)}_{n}$.

To approximate the desired passband support $\mathcal{K}_{n,m}$ given in (28), we adopt a simple solution in our design by choosing the polynomial coefficients to be

$$p(x_1,x_2,\ldots,x_n)=\begin{cases}1 & \text{if } \max_{i\le m}x_i>\max_{m<i\le n}x_i\\ 0 & \text{if } \max_{i\le m}x_i=\max_{m<i\le n}x_i\\ -1 & \text{otherwise}\end{cases}. \quad (30)$$

Table II displays the first two 3-D Bernstein polynomials obtained from (29) and (30) (with $m=1$ and $n=3$). After the change of variables, the resulting mapping kernel $K(e^{j\boldsymbol{\omega}})$ will have a maximally-flat frequency response, which converges to the desired ideal function $2\mathbb{1}_{\mathcal{K}_{m,n}}(\boldsymbol{\omega})-1$ with the increase of the order N. We omit here further description of these properties and refer readers to [28]–[30] for more details.

D. Design Example: 3-D Hourglass Filter Bank

In this example, we apply the proposed design techniques to construct an hourglass filter bank in 3-D. The 1-D polynomials $f_1(x)$ and $f_2(x)$ used in the design are generated from three lifting/ladder stages, whose coefficients are listed in Table I (under $n=3$). Recall from Fig. 3(a) that we need to use two mapping kernels to split the cascade tree. The first kernel, i.e.,

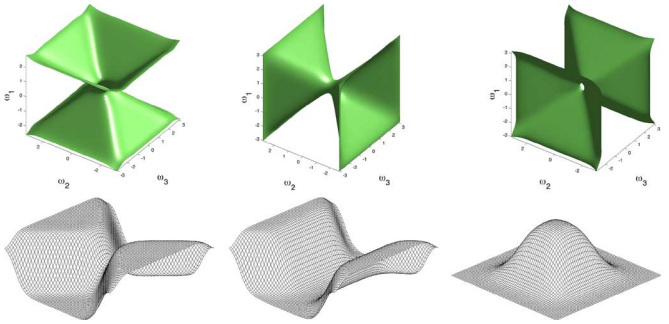

Fig. 9. Frequency responses of the designed 3-D filters. Top row (from left to right): the isosurfaces of three hourglass filters $H_1(e^{j\boldsymbol{\omega}})$, $H_2(e^{j\boldsymbol{\omega}})$, and $H_3(e^{j\boldsymbol{\omega}})$. Bottom row (from left to right): 2-D slices $H_1(e^{j(\omega_1,0,\omega_3)})$, $H_2(e^{j(\pi/2,\omega_2,\omega_3)})$, and $H_3(e^{j(\omega_1,\omega_2,\pi/3)})$.

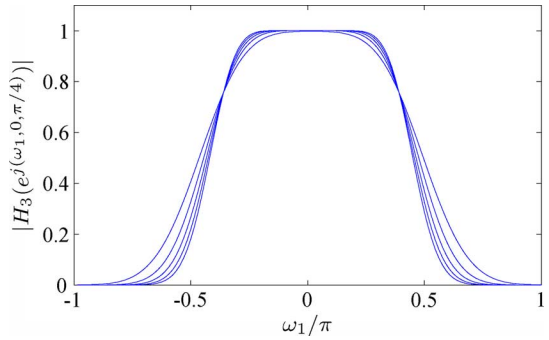

Fig. 10. 1-D frequency responses (taken along $\omega_2 = 0$ and $\omega_3 = 0.4\pi$) of $H_3(e^{j\boldsymbol{\omega}})$ obtained by choosing the order of the Bernstein polynomial to be $N = 6, 9, 12, 15$, and 18. Larger N leads to shaper frequency responses.

the one dividing the original spectrum into $\mathcal{H}_1$ and $\mathcal{H}_{\{2,3\}}$, is a 3-D filter; while the second kernel which further divides $\mathcal{H}_{\{2,3\}}$ is a 2-D filter operating on the (ω_2, ω_3) signal plane. All mapping kernels are designed using 3-D Bernstein polynomials according to (29) and (30). For simplicity, they all have the same order $N = 6$, though it is possible to use a different N for each kernel.

The resulting 3-D hourglass filters in the analysis part have support sizes as $37 \times 37 \times 37$, $25 \times 61 \times 61$, and $25 \times 49 \times 49$, respectively. Note that the actual implementation of the filter bank is based on the lifting/ladder structure illustrated in Fig. 7 and, as shown in Proposition 2 , takes much fewer number of arithmetic operations than a direct implementation with filters of the above sizes.

Fig. 9 presents the frequency responses of the designed 3-D hourglass filters. Only the analysis filters are shown and the synthesis filters are very similar. On the top row of Fig. 9 are the isosurfaces of the three filters, which closely resemble the ideal hourglass shapes. On the bottom row are several 2-D slices of the 3-D frequency responses. Depending on the locations of the cutting planes, the 2-D slices can have fan-shaped, trapezoid-shaped, or lowpass-shaped responses.

The order N of the Bernstein polynomials for mapping kernels can be used as a parameter to control the frequency responses of the 3-D hourglass filters. Fig. 10 shows the 1-D slices of $H_3(e^{j\boldsymbol{\omega}})$, designed by using different values of N. We can see that, by choosing a larger N, we can always sharpen the resulting frequency responses, but of course at the cost of increasing the spatial support sizes of the filters.

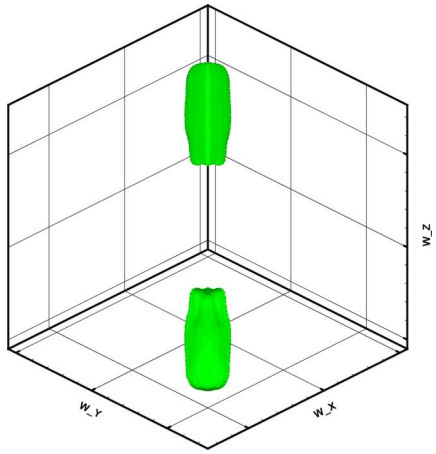

Fig. 11. The isosurface of the frequency support of one surfacelet subband. The 3-D hourglass filter bank designed in Section V-D is used to construct the surfacelet transform.

E. Multidimensional Directional Filter Banks and Video Denoising

An important application of the hourglass filter banks studied in this paper is the construction of multidimensional directional filter banks (called the surfacelet transform in [10]). We show in Fig. 11 the isosurface of the frequency support of one surfacelet subband, which is obtained by the concatenation of a multiscale pyramid, a 3-D hourglass filter bank such as the one designed in Section V-D, and a sequence of critically sampled checkerboard filter banks [10]. Compared to the frequency supports of the hourglass filters, the 3-D surfacelet filter bank provides a much finer directional partitioning of the frequency spectrum, and thus offering higher angular resolution.

Finally, we demonstrate a potential application of the 3-D hourglass filter bank and its generalization — the surfacelet transform — to video processing. Fig. 12(a) and (b) displays a single frame from the image sequence "Coast Guard" and its noisy version contaminated by zero-mean white Gaussian noise. Applying the surfacelet transform to the noisy video, we then try to reduce the noise by first truncating the transform coefficients with a fixed threshold, and then taking the inverse transform via the synthesis filter bank. See [10] for more details on this simple denoising scheme.

In Fig. 12(c) and (d), we use Surfacelet-FIR and Surfacelet-FREQ to differentiate between the denoising results from two versions of the surfacelet transform: the former uses the hourglass filters designed in Section V-D, while the latter uses hourglass filters designed in the frequency domain [10]. For benchmark, we also show in Fig. 12(e) and (f) the results obtained by using the real-valued dual-tree wavelet transform (DTWT) [32], [33] and the 3-D undecimated wavelet transform (UDWT).

We can see that Surfacelet-FIR and Surfacelet-FREQ share fairly similar performance. The advantage of using Surfacelet-FIR is that the hourglass filter banks can be implemented by FIR filters. Among DTWT, UDWT, and Surfacelet-FIR, the surfacelet transform using filters designed in this paper outperforms the other two 3-D transforms by a large margin (up to 0.76 dB) on the test sequence, which suggests the potential of the surfacelet transform in video processing.

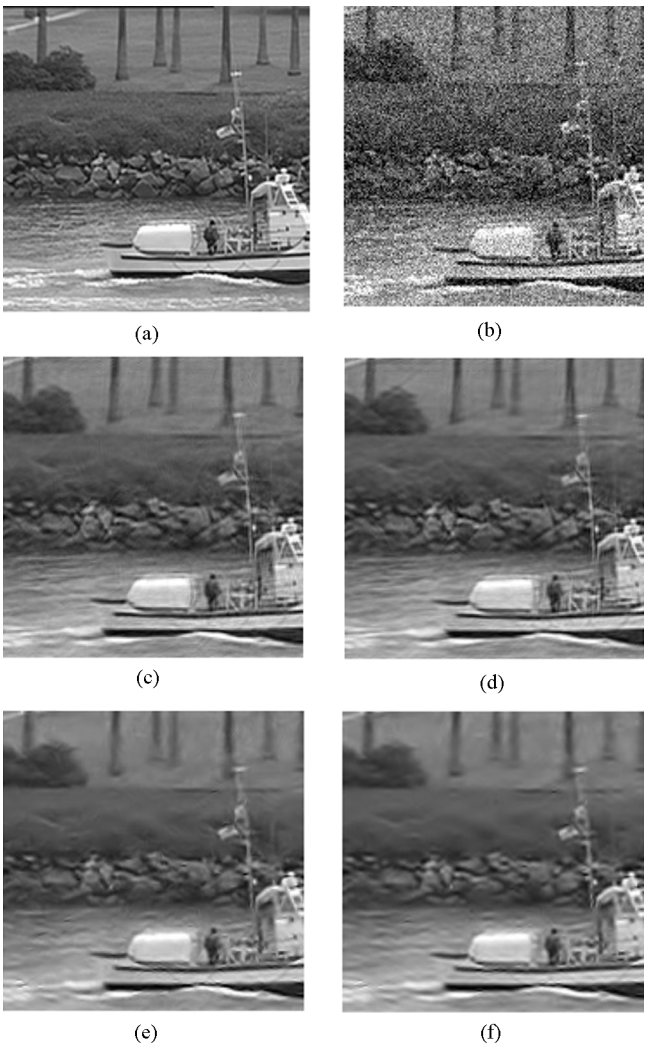

Fig. 12. Comparisons of video denoising results by using different transforms. The PSNR values are averaged across the entire image sequence. (a) Original frame. (b) Noisy frame (PSNR = 18.62 dB). (c) Surfacelet-FIR (PSNR = 26.75 dB). (d) Surfacelet-FREQ (PSNR = 26.84 dB). (e) DTWT (PSNR = 26.09 dB). (f) UDWT (PSNR = 25.99 dB).

VI. Conclusion

In this paper, we proposed a novel mapping-based design for multidimensional nonsubsampled hourglass filter banks, featuring perfect reconstruction, FIR filters, efficient implementation using lifting/ladder structures, and a near-tight frame construction. A key advantage of the design is that it is easily extended to arbitrary dimensions. As an important issue in the proposed mapping-based scheme, we study conditions on the class of mapping kernels which lead to good frequency responses when the filters used are nonideal. Among all possible choices, we then propose an optimal specification for the kernels that leads to the simplest passband shapes and involves the fewest number of frequency variables. In addition to the video denoising example shown in the paper, we envision that the designed multidimensional hourglass filter banks would find applications in various areas that involve the directional analysis of multidimensional volumetric data, including seismic image processing and medical image analysis.

Appendix I
Proof of Lemma 2

We can expand the first equivalent filter $F_{\Lambda_1}(e^{j\boldsymbol{\omega}})$ as follows:

$$\begin{aligned}
&F_{\Lambda_1}(e^{j\boldsymbol{\omega}}) \\
&\quad = F_{\Lambda}(e^{j\boldsymbol{\omega}})\, F_1(e^{j\boldsymbol{\omega}}) \\
&\quad = (\mathbb{1}_{\mathcal{H}_\Lambda}(\boldsymbol{\omega}) + \mathcal{E}_\epsilon(\boldsymbol{\omega}) + \mathcal{T}_{\partial\mathcal{H}_\Lambda + B_\delta}(\boldsymbol{\omega})) \\
&\qquad \cdot (\mathbb{1}_{\mathcal{K}}(\boldsymbol{\omega}) + \mathcal{E}_\epsilon(\boldsymbol{\omega}) + \mathcal{T}_{\partial\mathcal{K} + B_\delta}(\boldsymbol{\omega})) \\
&\quad = \mathbb{1}_{\mathcal{H}_\Lambda \cap \mathcal{K}}(\boldsymbol{\omega}) + \underbrace{\mathcal{E}_\epsilon(\boldsymbol{\omega})\, F_1(e^{j\boldsymbol{\omega}}) + \mathcal{E}_\epsilon(\boldsymbol{\omega}) \left(F_\Lambda(e^{j\boldsymbol{\omega}}) - \mathcal{E}_\epsilon(\boldsymbol{\omega})\right)}_{\text{in-band ripples}} \\
&\qquad + \underbrace{\mathbb{1}_{\mathcal{H}_\Lambda}(\boldsymbol{\omega})\, \mathcal{T}_{\partial\mathcal{K} + B_\delta}(\boldsymbol{\omega}) + \mathbb{1}_{\mathcal{K}}(\boldsymbol{\omega})\, \mathcal{T}_{\partial\mathcal{H}_\Lambda + B_\delta}(\boldsymbol{\omega})}_{\text{first transition band}} \\
&\qquad + \underbrace{\mathcal{T}_{\partial\mathcal{H}_\Lambda + B_\delta}(\boldsymbol{\omega})\, \mathcal{T}_{\partial\mathcal{K} + B_\delta}(\boldsymbol{\omega})}_{\text{second transition band}}. \qquad (31)
\end{aligned}$$

For the term related to in-band ripples, we have

$$\begin{aligned}
&\left|\mathcal{E}_\epsilon(\boldsymbol{\omega})\, F_1(e^{j\boldsymbol{\omega}}) + \mathcal{E}_\epsilon(\boldsymbol{\omega}) \left(F_\Lambda(e^{j\boldsymbol{\omega}}) - \mathcal{E}_\epsilon(\boldsymbol{\omega})\right)\right| \\
&\qquad \le \epsilon(1+\epsilon) + \epsilon(1+2\epsilon) = \epsilon(2+3\epsilon).
\end{aligned}$$

Based on the assumption that $\epsilon \ll 1$, we can omit the second-order term and get

$$\mathcal{E}_\epsilon(\boldsymbol{\omega})\, F_1(e^{j\boldsymbol{\omega}}) + \mathcal{E}_\epsilon(\boldsymbol{\omega}) \left(F_\Lambda(e^{j\boldsymbol{\omega}}) - \mathcal{E}_\epsilon(\boldsymbol{\omega})\right) \approx 2\,\mathcal{E}_\epsilon(\boldsymbol{\omega}). \quad (32)$$

Note that $\mathcal{E}_\epsilon(\boldsymbol{\omega})$ in both sides of the equation above represent different instances of a class of functions.

We can rewrite the first term on transition band in (31) as $\mathcal{T}_{(\mathcal{H}_\Lambda \cap (\partial\mathcal{K} + B_\delta)) \cup (\mathcal{K} \cap (\partial\mathcal{H}_\Lambda + B_\delta))}(\boldsymbol{\omega})$. For $\delta \ll 1$, the support of this bump function can be approximated as

$$\begin{aligned}
&(\mathcal{H}_\Lambda \cap (\partial\mathcal{K} + B_\delta)) \cup (\mathcal{K} \cap (\partial\mathcal{H}_\Lambda + B_\delta)) \\
&\quad \approx ((\mathcal{H}_\Lambda \cap \partial\mathcal{K}) + B_\delta) \cup ((\mathcal{K} \cap \partial\mathcal{H}_\Lambda) + B_\delta) \\
&\quad = (\mathcal{H}_\Lambda \cap \partial\mathcal{K}) \cup (\mathcal{K} \cap \partial\mathcal{H}_\Lambda) + B_\delta = \partial(\mathcal{H}_\Lambda \cap \mathcal{K}) + B_\delta. \qquad (33)
\end{aligned}$$

Similarly, for $\delta \ll 1$, we can rewrite the second term on transition band in (31) as

$$\mathcal{T}_{\partial\mathcal{H}_\Lambda + B_\delta}(\boldsymbol{\omega})\, \mathcal{T}_{\partial\mathcal{K} + B_\delta}(\boldsymbol{\omega}) \approx \frac{1}{2} \mathcal{T}_{\partial\mathcal{H}_\Lambda \cap \partial\mathcal{K} + B_\delta}(\boldsymbol{\omega}). \quad (34)$$

Substituting the corresponding terms in (31) with (32), (33), and (34), we get the expression in (17). The expression for the second equivalent filter $F_{\Lambda \setminus \Lambda_1}(e^{j\boldsymbol{\omega}})$ in (18) can also be obtained by following the same line of derivations as above, and using the fact that $\partial(\mathcal{K}^C) = \partial\mathcal{K}$.

Appendix II
Proof of Proposition 1

We first show that $\mathcal{K}_{\Lambda,\Lambda_1}$ indeed satisfies the conditions given in (19) and (20). Due to the periodicity of the passband supports, we only consider the situations when $\boldsymbol{\omega} \in (-\pi, \pi]^d$.

Condition (19) can be verified as follows:

$$\begin{aligned}
&\mathcal{H}_\Lambda \cap \mathcal{K}_{\Lambda,\Lambda_1} \\
&\quad = \{\max_{i \in \Lambda} |\omega_i| = \max_{1 \le i \le d} |\omega_i|\} \cap \{\max_{i \in \Lambda_1} |\omega_i| = \max_{i \in \Lambda} |\omega_i|\} \\
&\quad = \{\max_{i \in \Lambda_1} |\omega_i| = \max_{1 \le i \le d} |\omega_i|\} = \mathcal{H}_{\Lambda_1}.
\end{aligned}$$

For the boundary condition in (20), we first notice that, equivalent to the formulation given in Lemma 1, we can also write $\mathcal{H}_\Lambda = \{\max_{i\in\Lambda} |\omega_i| \geq \max_{i\in\Lambda^C} |\omega_i|\}$, where $\Lambda^C \stackrel{\text{def}}{=} \{1,2,\ldots,d\}\backslash\Lambda$ is the complement of Λ. It then follows that the boundary of $\mathcal{H}_\Lambda$ can be calculated as $\partial\mathcal{H}_\Lambda = \{\max_{i\in\Lambda} |\omega_i| = \max_{i\in\Lambda^C} |\omega_i|\}$. Similarly, $\partial\mathcal{K}_{\Lambda,\Lambda_1} = \{\max_{i\in\Lambda_1} |\omega_i| = \max_{i\in\Lambda\backslash\Lambda_1} |\omega_i|\}$. Now we have

$$\begin{aligned}
&\partial\mathcal{H}_\Lambda \cap \partial\mathcal{K}_{\Lambda,\Lambda_1} \\
&\quad = \{\max_{i\in\Lambda} |\omega_i| = \max_{i\in\Lambda^C} |\omega_i|\} \cap \{\max_{i\in\Lambda_1} |\omega_i| = \max_{i\in\Lambda\backslash\Lambda_1} |\omega_i|\} \\
&\quad = \{\max_{i\in\Lambda_1} |\omega_i| = \max_{i\in\Lambda\backslash\Lambda_1} |\omega_i| = \max_{i\in\Lambda^C} |\omega_i|\} \\
&\quad \subset \{\max_{i\in\Lambda_1} |\omega_i| = \max_{i\in\Lambda_1^C} |\omega_i|\} \\
&\qquad \cap \{\max_{i\in\Lambda\backslash\Lambda_1} |\omega_i| = \max_{i\in(\Lambda\backslash\Lambda_1)^C} |\omega_i|\} \\
&\quad = \partial\mathcal{H}_{\Lambda_1} \cap \partial\mathcal{H}_{\Lambda\backslash\Lambda_1}.
\end{aligned}$$

To verify (22), we first write, without loss of generality, any boundary facet $\mathcal{B}$ of $\mathcal{K}_{\Lambda,\Lambda_1}$ as

$$\mathcal{B} = \{\omega_{i_0} = \max_{i\in\Lambda_1} |\omega_i| = \max_{j\in\Lambda\backslash\Lambda_1} |\omega_j| = \omega_{j_0}\},$$

for some $i_0 \in \Lambda_1$ and $j_0 \in \Lambda \setminus \Lambda_1$. We can then check that

$$\begin{aligned}
&\mathcal{B} \cap \mathcal{H}_\Lambda \\
&= \{\omega_{i_0} = \max_{i\in\Lambda_1} |\omega_i| = \max_{j\in\Lambda\backslash\Lambda_1} |\omega_j| = \omega_{j_0}\} \\
&\quad \cap \{\max_{i\in\Lambda} |\omega_i| = \max_{1\leq i\leq d} |\omega_i|\} \\
&\subset \{\max_{i\in\Lambda_1} |\omega_i| = \max_{i\in\Lambda_1^C} |\omega_i|\}
\end{aligned}$$

is a nonempty boundary facet of $\mathcal{H}_{\Lambda_1}$, but lies within the interior of $\mathcal{H}_\Lambda$. For any $\mathcal{K}$ that satisfies the design requirement (20), the condition $\mathcal{H}_\Lambda \cap \mathcal{K} = \mathcal{H}_{\Lambda_1}$ implies that $\partial\mathcal{H}_{\Lambda_1} \subseteq \partial\mathcal{H}_\Lambda \cup \partial\mathcal{K}$, i.e., any boundary facet of $\mathcal{H}_{\Lambda_1}$ must either come from $\partial\mathcal{H}_\Lambda$ or $\partial\mathcal{K}$. Since $\mathcal{B} \cap \mathcal{H}_\Lambda$ belongs to a boundary facet of $\partial\mathcal{H}_{\Lambda_1}$ but lies in the interior of $\mathcal{H}_\Lambda$, it must be from $\partial\mathcal{K}$, i.e., $\mathcal{B} \cap \mathcal{H}_\Lambda \subseteq \partial\mathcal{K}$.

Appendix III
Proof of Proposition 3

Applying the Cauchy-Schwarz inequality to the perfect reconstruction condition of the filter bank yields

$$\begin{aligned}
1 &= \sum_{i=1}^{d} H_i(e^{j\boldsymbol{\omega}})\, G_i(e^{j\boldsymbol{\omega}}) \\
&\leq \left(\sum_{i=1}^{d} |H_i(e^{j\boldsymbol{\omega}})|^2\right)^{1/2} \left(\sum_{i=1}^{d} |G_i(e^{j\boldsymbol{\omega}})|^2\right)^{1/2}, \text{ for all } \boldsymbol{\omega}. \quad (35)
\end{aligned}$$

Since the filter bank uses FIR filters, all the frequency responses are then continuous functions, whose minimum and maximum values can always be achieved. In particular, we can find some $\boldsymbol{\omega}_0$ such that

$$\sum_{i=1}^{d} |H_i(e^{j\boldsymbol{\omega}_0})|^2 = \min_{\boldsymbol{\omega}} \sum_{i=1}^{d} |H_i(e^{j\boldsymbol{\omega}})|^2 = A_E.$$

Evaluating (35) at frequency $\boldsymbol{\omega}_0$ leads to

$$1 \leq \sqrt{A_E} \left(\sum_{i=1}^{d} |G_i(e^{j\boldsymbol{\omega}_0})|^2\right)^{1/2} \leq \sqrt{A_E}\sqrt{B_R}.$$

Similarly, we can show that $1 \leq \sqrt{B_E}\sqrt{A_R}$. Combining these two inequalities, we get $1 \leq \sqrt{A_E B_E A_R B_R}$, which implies that

$$1 \leq \sqrt{\frac{B_E}{A_E}\frac{B_R}{A_R}} \leq B_E\, B_R. \quad (36)$$

In calculating $B_E = \max_{\boldsymbol{\omega}} \sum_{i=1}^{d} |H_i(\boldsymbol{\omega})|^2$, recall that the analysis filters $H_i(e^{j\boldsymbol{\omega}})$ are obtained as a concatenation of two-channel filter banks whose component filters are of the form $f_1(K(e^{j\boldsymbol{\omega}}))$ and $f_2(K(e^{j\boldsymbol{\omega}}))$. In the 2-D (i.e., two-channel) case, since $\sup_{\boldsymbol{\omega}} |K(e^{j\boldsymbol{\omega}})| \leq 1$, then

$$\begin{aligned}
B_E &= \max_{\boldsymbol{\omega}} \left(f_1^2(K(e^{j\boldsymbol{\omega}})) + f_2^2(K(e^{j\boldsymbol{\omega}}))\right) \\
&\leq \max_{|x|\leq 1} \left(f_1^2(x) + f_2^2(x)\right). \quad (37)
\end{aligned}$$

Meanwhile, since $e_1(x) = f_2(-x)$ and $e_2(x) = f_1(-x)$, we have $1 = f_1(0)e_1(0) + f_2(0)e_2(0) = 2f_1(0)f_2(0) \leq f_1^2(0) + f_2^2(0)$, and therefore

$$\max_{|x|\leq 1} \left(f_1^2(x) + f_2^2(x)\right) \geq 1. \quad (38)$$

In the general d-D case, we have a total of $\lceil \log_2(d) \rceil$ levels of concatenation of two-channel filter banks. Applying (37) and (38), and by induction, we get

$$B_E = \max_{\boldsymbol{\omega}} \sum_{i=1}^{d} |H_i(\boldsymbol{\omega})|^2 \leq \max_{|x|\leq 1} \left(f_1^2(x) + f_2^2(x)\right)^{\lceil \log_2(d) \rceil}. \quad (39)$$

Similarly, we can show that

$$B_R = \max_{\boldsymbol{\omega}} \sum_{i=1}^{d} |G_i(\boldsymbol{\omega})|^2 \leq \max_{|x|\leq 1} \left(f_1^2(x) + f_2^2(x)\right)^{\lceil \log_2(d) \rceil}. \quad (40)$$

Linking the inequalities in (36), (39), and (40) leads to the result in the proposition.

References

[1] R. Ansari, "Efficient IIR and FIR fan filters," *IEEE Trans. Circuits Syst.*, vol. CAS-34, no. 8, pp. 941–945, Aug. 1987.

[2] D. B. H. Tay and N. Kingsbury, "Flexible design of multidimensional perfect reconstruction FIR 2-band filters using transformations of variables," *IEEE Trans. Image Process.*, vol. 2, no. 4, pp. 466–480, Oct. 1993.

[3] S.-M. Phoong, C. W. Kim, P. P. Vaidyanathan, and R. Ansari, "A new class of two-channel biorthogonal filter banks and wavelet bases," *IEEE Trans. Signal Process.*, vol. 43, no. 3, pp. 649–665, Mar. 1995.

[4] K. S. C. Pun and T. Q. Nguyen, "A novel and efficient design of multidimensional PR two-channel filter banks with hourglass-shaped passband support," *IEEE Signal Process. Lett.*, vol. 11, no. 3, pp. 345–348, Mar. 2004.

[5] T. T. Nguyen and S. Oraintara, "Efficient implementation of undecimated directional filter banks," in *Proc. Europ. Signal Process. Conf. EUSIPCO)*, Florence, Italy, Sep. 2006.

[6] A. L. Cunha, J. Zhou, and M. N. Do, "The nonsubsampled contourlet transform: Theory, design and applications," *IEEE Trans. Image Process.*, vol. 15, no. 10, pp. 3089–3101, Oct. 2006.

[7] R. H. Bamberger and M. J. T. Smith, "A filter bank for the directional decomposition of images: Theory and design," *IEEE Trans. Signal Process.*, vol. 40, no. 4, pp. 882–893, Apr. 1992.
[8] S. Park, M. J. T. Smith, and R. M. Mersereau, "Improved structures of maximally decimated directional filter banks for spatial image analysis," *IEEE Trans. Image Process.*, vol. 13, no. 11, pp. 1424–1431, Nov. 2004.
[9] M. N. Do, "Directional multiresolution image representations," Ph.D., Swiss Federal Inst. Technol., Lausanne, 2001.
[10] Y. M. Lu and M. N. Do, "Multidimensional directional filter banks and surfacelets," *IEEE Trans. Image Process.*, vol. 16, no. 4, pp. 918–931, Apr. 2007.
[11] G. Runze, "Efficient design of digital 3-D cone-shaped FIR fan-filters using transformation," in *Proc. 10th IEEE Workshop on Image and Multidimens. Signal Process.*, Alpbach, Austria, Jul. 1998, pp. 263–266.
[12] S. Park, "New directional filter banks and their applications in image processing," Ph.D., Georgia Inst. Technol., Atlanta, 1999.
[13] L. T. Bruton, "Three-dimensional cone filter banks," *IEEE Trans. Circuits Syst. I*, vol. 50, no. 2, pp. 208–216, Feb. 2003.
[14] R. H. Bamberger, "New results on two and three dimensional directional filter banks," in *27th Asilomar Conf. Signals, Syst. Comp.*, 1993, vol. 2, pp. 1286–1290.
[15] Y. M. Lu and M. N. Do, *On the Lattice Tiling of 3-D Hourglass-Shaped Frequency Regions*, 2006, unpublished.
[16] F. Bruekers and A. W. M. van der Enden, "New networks for perfect inversion and perfect reconstruction," *IEEE J. Sel. Areas Commun.*, vol. 10, no. 1, pp. 129–137, Jan. 1992.
[17] W. Sweldens, "The lifting scheme: A custom-design construction of biorthogonal wavelets," *Appl. Comput. Harmonic Analysis*, vol. 3, no. 2, pp. 186–200, 1996.
[18] P. P. Vaidyanathan, *Multirate Systems and Filter Banks*. Englewood Cliffs: Prentice Hall, 1993.
[19] M. Vetterli and J. Kovačević, *Wavelets and Subband Coding*. Englewood Cliffs: Prentice Hall, 1995.
[20] J. H. McClellan, "The design of two-dimensional digital filters by transformation," in *Proc. 7th Ann. Princeton Conf. Inf. Sci. Syst.*, Princeton, NJ, Mar. 1973, pp. 247–251.
[21] J. Kovačević and M. Vetterli, "Nonseparable multidimensional perfect reconstruction filter banks and wavelet bases for $\mathcal{R}^n$," *IEEE Trans. Inf. Theory*, vol. 38, no. 2, pp. 533–555, Mar. 1992.
[22] I. A. Shah and A. A. C. Kalker, "Theory and design of multidimensional QMT sub-band filters from 1-D filters and polynomials using transforms," *Inst. Elect. Eng. Proc. I: Commun., Speech Vision*, vol. 140, no. 1, pp. 67–71, Feb. 1993.
[23] H. Bölcskei, F. Hlawatsch, and H. G. Feichtinger, "Frame-theoretic analysis of oversampled filter banks," *IEEE Trans. Signal Process.*, vol. 46, no. 12, pp. 3256–3268, Dec. 1998.
[24] Z. Cvetković and M. Vetterli, "Oversampled filter banks," *IEEE Trans. Signal Process.*, vol. 46, no. 5, pp. 1245–1255, May 1998.
[25] J. Kovačević, P. L. Dragotti, and V. K. Goyal, "Filter bank frame expansions with erasures," *IEEE Trans. Inf. Theory*, vol. 48, no. 6, pp. 1439–1450, Jun. 2002.
[26] A. E. Cetin and R. Ansari, "An iterative procedure for designing two dimensional FIR filters," in *Proc. IEEE Int. Symp. Circuits Syst.*, Philadelphia, PA, 1987, pp. 1044–1047.
[27] R. Ansari and A. E. Cetin, "Two-dimensional FIR filters," in *The Circuits and Filters Handbook*, W.-K. Chen, Ed. Boca Raton: CRC, 1995, pp. 2732–2761.
[28] H. Caglar and A. N. Akansu, "A generalized parametric PR-QMF design technique based on Bernstein polynomial approximation," *IEEE Trans. Signal Process.*, vol. 41, no. 7, pp. 2314–2321, Jul. 1993.
[29] T. Cooklev, T. Yoshida, and A. Nishihara, "Maximally flat half-band diamond-shaped FIR filters using the Bernstein polynomial," *IEEE Trans. Circuits Syst. II*, vol. 40, pp. 749–751, Nov. 1993.
[30] D. B. H. Tay, "Parametric Bernstein polynomial for least squares design of 3-D wavelet filter banks," *IEEE Trans. Circuits Syst. I*, vol. 49, pp. 887–891, Jun. 2002.
[31] P. J. Davis, *Interpolation and Approximation*. New York: Blaisdell, 1963.
[32] N. Kingsbury, "Complex wavelets for shift invariant analysis and filtering of signals," *Appl. Comput. Harmonic Anal.*, vol. 10, pp. 234–253, 2001.
[33] I. W. Selesnick, "The double-density dual-tree DWT," *IEEE Trans. Signal Process.*, vol. 52, no. 5, pp. 1304–1314, May 2004.

Yue M. Lu (S'04–M'08) received the B.Eng. and M.Eng. degrees in electrical engineering from Shanghai Jiao Tong University, China, in 1999 and 2002, respectively. He received the M.Sc. degree in mathematics and the Ph.D. degree in electrical engineering from the University of Illinois at Urbana-Champaign in 2007.

He was a Research Assistant with the University of Illinois at Urbana-Champaign, and has worked for Microsoft Research Asia, Beijing, China, and Siemens Corporate Research, Princeton, NJ. He is now with the Audio-Visual Communications Laboratory, Swiss Federal Institute of Technology Lausanne (EPFL), Switzerland. His research interests include the theory, constructions, and applications of multiscale geometric representations for multidimensional signals; image and video processing; and sampling theories.

Dr. Lu received the Most Innovative Paper Award of IEEE International Conference on Image Processing (ICIP) in 2006 for his paper (with Minh N. Do) on the construction of directional multiresolution image representations, and the Student Paper Award of IEEE ICIP in 2007.

Minh N. Do (M'02–SM'07) was born in Thanh Hoa, Vietnam, in 1974. He received the B.Eng. degree in computer engineering from the University of Canberra, Australia, in 1997, and the Dr.Sci. degree in communication systems from the Swiss Federal Institute of Technology Lausanne (EPFL), Switzerland, in 2001.

Since 2002, he has been an Assistant Professor with the Department of Electrical and Computer Engineering and a Research Assistant Professor with the Coordinated Science Laboratory and the Beckman Institute, University of Illinois at Urbana-Champaign (UIUC). His research interests include image and multi-dimensional signal processing, wavelets and multiscale geometric analysis, computational imaging, and visual information representation.

Dr. Do received a Silver Medal from the Thirty-Second International Mathematical Olympiad in 1991, a University Medal from the University of Canberra in 1997, the Best Doctoral Thesis Award from EPFL in 2001, and a CAREER award from the National Science Foundation in 2003. He was named a Beckman Fellow at the Center for Advanced Study, UIUC, in 2006 and received a Xerox Award for Faculty Research from the College of Engineering, UIUC, in 2007. He is a member of the IEEE Signal Processing Society Signal Processing Theory and Methods and Image and MultiDimensional Signal Processing Technical Committees, and an Associate Editor of the IEEE TRANSACTIONS ON IMAGE PROCESSING.